Effective intermediate-spin iron in O$_2$-transporting heme proteins

Nils Schuth[a], Stefan Mebs[a], Dennis Huwald[b], Pierre Wrzolek[c], Matthias Schwalbe[c], Anja Hemschemeier[b], and Michael Haumann[a,1]

[a]Department of Physics, Freie Universität Berlin, 14195 Berlin, Germany; [b]Department of Plant Biochemistry, Section of Photobiotechnology, Ruhr-Universität Bochum, 44801 Bochum, Germany; and [c]Department of Chemistry, Humboldt-Universität zu Berlin, 12489 Berlin, Germany

Proteins carrying an iron-porphyrin (heme) cofactor are essential for biological O$_2$ management. The nature of Fe-O$_2$ bonding in hemoproteins is debated for decades. We used energy-sampling and rapid-scan X-ray Kβ emission and K-edge absorption spectroscopy as well as quantum chemistry to determine molecular and electronic structures of unligated (deoxy), CO-inhibited (carboxy), and O$_2$-bound (oxy) hemes in myoglobin (MB) and hemoglobin (HB) solutions and in porphyrin compounds at 20–260 K. Similar metrical and spectral features revealed analogous heme sites in MB and HB and the absence of low-spin (LS) to high-spin (HS) conversion. Amplitudes of Kβ main-line emission spectra were directly related to the formal unpaired Fe(d) spin count, indicating HS Fe(II) in deoxy and LS Fe(II) in carboxy. For oxy, two unpaired Fe(d) spins and, thus by definition, an intermediate-spin iron center, were revealed by our static and kinetic X-ray data, as supported by (time-dependent) density functional theory and complete-active-space self-consistent-field calculations. The emerging Fe-O$_2$ bonding situation includes in essence a ferrous iron center, minor superoxide character of the noninnocent ligand, significant double-bond properties of the interaction, and three-center electron delocalization as in ozone. It resolves the apparently contradictory classical models of Pauling, Weiss, and McClure/Goddard into a unifying view of O$_2$ bonding, tuned toward reversible oxygen transport.

heme cofactor | X-ray spectroscopy | quantum chemistry | O$_2$ binding | spin state

Proteins binding an iron-porphyrin (heme) cofactor are nature's versatile dioxygen (O$_2$) managers, facilitating O$_2$ sensing, transport, activation chemistry, and catalysis (1). Scrutiny over decades has been devoted to the heme chemistry in myoglobin (MB) and hemoglobin (HB) proteins of vertebrates (Fig. 1), which is the basis for their vital O$_2$-transporting properties (1–5). Renewed interest in the topic stems from ongoing discovery of globins in plants and microorganisms, which further extends the spectrum of biological functions (6–8). A controversy remains on the nature of the iron-oxygen bonding in HB/MB, dating back to pioneering work of Pauling, Monod, and Perutz starting in the 1930s (3, 9).

Three physiologically relevant heme species are distinguished in MB/HB for which crystal structures at ~1 Å resolution are available (10, 11): the ligand-free (deoxy), carbon-monoxide inhibited (carboxy), and O$_2$-bound (oxy) forms (Fig. 1), besides the ferric (met) species resulting from autoxidation. Paramagnetic behavior has established high-spin (HS) iron in deoxy [d^6 Fe(II); spin (S) multiplicity, M = 2S + 1 = 5] and met [d^5 Fe(III); M = 6], but carboxy is diamagnetic because of low-spin (LS) Fe(II) (M = 1) (12). For oxy, a diamagnetic (M = 1) cofactor was proven (3, 12, 13). However, the O$_2$ triplet ground state provides several options for spin flipping or charge transfer (Fig. 1): Pauling suggested a neutral singlet O$_2$ bound to a formal LS Fe(II) (13, 14), McClure suggested a triplet O$_2$ and an intermediate-spin (IS) Fe(II) with antiferromagnetic (afc) coupling (15), an IS Fe(II) with d-level population inversion in an ozone-like model was also suggested by Goddard (16), and Weiss suggested an Fe(III) afc coupled to a superoxo (O$_2^{\cdot-}$) ligand (17). The possible resonance character of these Lewis structures was emphasized already in early theory work (18). Density functional theory (DFT), providing access to

experimental observables (19, 20), and complete-active-space self-consistent-field (CASSCF) quantum chemical calculations facilitated description of many structural and spectroscopic features of the O$_2$ bonding (1, 18). A McClure-like oxy (21), and Pauling/Weiss formulations have emerged, to some extent depending on model terms used to interpret multiconfigurational wavefunctions (21–23). Modification of porphyrin groups and heme/ligand geometries by the protein matrix and hydrogen bonding may bias the Fe–O$_2$ interaction to the diverse functions (1, 24–26).

Core level spectroscopy is powerful for electronic structure analysis of transition metal complexes (27, 28). X-ray absorption spectroscopy (XAS) probes unoccupied valence levels by resonant 1s electron excitation in the pre-K-edge region (core-to-valence transitions, ctv), ligation symmetries in the X-ray absorption near edge structure (XANES), and bond lengths in the extended X-ray absorption fine structure (EXAFS). X-ray emission spectroscopy (XES) of the Kβ line probes occupied levels via electronic decay from metal-3p (main lines) or metal-valence (satellite lines; valence-to-core transitions, vtc) levels to the core hole (29). The core/valence-to-core electronic transitions (ctv/vtc) spectra can be calculated by DFT methods for theory benchmarking (30, 31). 3p-3d spin coupling splits the Kβ main-line emission into the Kβ' and Kβ$_{1,3}$ features, and the Kβ' intensity is a measure of the metal spin state and bonding covalency (32–34). XAS has been used to address structural metrics, solution vs. crystalline materials, and redox states in MB/HB (35–39). ctv data were interpreted in favor of the Weiss model of O$_2$ binding (36, 40). Systematic Kβ XES on hemoproteins has not been done yet and is challenging on protein solutions because of radiation-induced modifications (41). Temperature effects further may contribute, because in met MB/HB partial spin crossover (i.e., HS population) was found (42).

We used advanced X-ray spectroscopy to study heme species in MB and HB proteins in solution. Structural and electronic features

Significance

Tuning of the iron-oxygen bonding in hemoproteins is crucial for their versatile O$_2$ chemistry. The nature of the Fe-O$_2$ bond in myoglobin (MB) and hemoglobin (HB) has been debated for a long time. High-resolution X-ray Kβ emission and K-edge absorption spectroscopy on MB and HB solutions and quantum chemical (time-dependent) density functional theory and complete-active-space self-consistent-field calculations revealed an essentially ferrous, intermediate-spin iron in an ozone-like configuration in O$_2$-bound oxy heme. The emerging bonding situation resolves the three classical models into a consistent view of the metal–ligand interaction, biased toward reversible O$_2$ binding in the oxygen transporters.
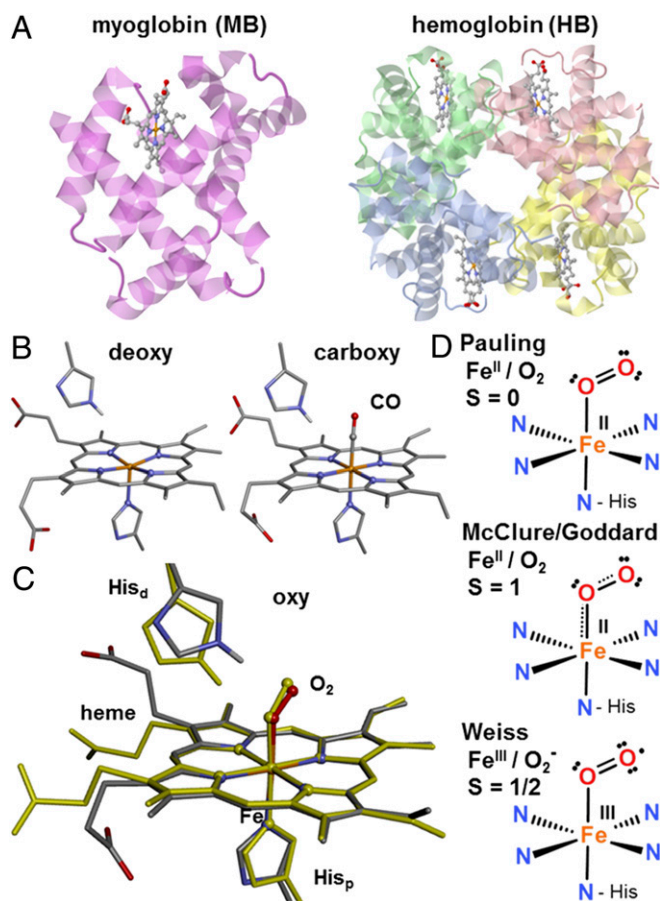
Fig. 1. Heme protein structures and O_2 binding. (*A*) Crystal structures of human MB/HB (*Left/Right*, PDB ID codes 2DN2/3RGK). (*B*) Structures of deoxy/carboxy hemes in MB (PDB ID codes 3QM6/3QM7, 0.91/0.96 Å resolution). (*C*) Overlay of oxy hemes in MB/HB (balls-and-sticks/yellow-sticks, PDB ID codes 1A6M/2DN1, 1.00/1.25 Å resolution). (*D*) Schematic Fe-O_2 bonding in oxy in the three literature models (His$_{p/d}$ in *C*, proximal/distal histidine; color code: gray, C; blue, N; red, O; orange, Fe). Hydrogen bonding of His$_d$ to bound O_2 has been established by neutron diffraction (68).

were similar for both proteins and constant at 20–260 K. Static and kinetic X-ray absorption/emission spectroscopy (XAS/XES) and (time-dependent) density functional theory (TDDFT) and CASSCF analyses revealed HS Fe(II) in deoxy, LS Fe(II) in carboxy, and IS iron in a delocalized Fe-O_2 bonding situation in oxy, which resolves the classical models in a unifying view of the metal–ligand interaction.

Results

Heme Species Quantification. MB and HB proteins in solution were prepared with ligand-free (deoxy), carbon monoxide inhibited (carboxy), or oxygenated (oxy) hemes. Similar optical absorption spectra of MB and HB (*SI Appendix*, Fig. S2) with typical Soret band shifts (MB/HB: met, 407/405 nm; deoxy, 433/429 nm; carboxy, 423/419 nm; oxy, 419/414 nm) and differences in the Q-band region (500–600 nm) agreed with previous reports (36, 43). Fe K-edge XANES spectra of three sets of MB/HB samples were collected at 20 K and 260 K at two monochromator resolutions and using broad-band Kα or narrow-band Kβ emission detection (*SI Appendix*, Figs. S3–S5). XANES shapes of MB/HB differed only slightly, and K-edge energies of MB/HB for a given heme species at 20/260 K were similar within ±0.1 eV (deoxy, 7,121.0 eV; carboxy, 7,122.3 eV; oxy, 7,123.9 eV; *SI Appendix*, Table S1), in agreement with previous reports (35, 36, 40). The ~1.3 eV or ~2.9 eV energy differences for deoxy/carboxy or deoxy/oxy reflected iron ligation and spin-state changes as outlined below. Precise iron-ligand bond

lengths were determined from EXAFS analysis. Coordination numbers close to unity were found for the Fe-CO and Fe-O_2 bonds in MB/HB. The Fe-O_2 (1.90 Å), Fe-CO (1.79 Å), Fe-N$_{porphyrin}$ (deoxy, 2.07 Å; carboxy, 2.01 Å; oxy, 2.04 Å), and Fe-H$_{His}$ (deoxy, 2.18 Å; carboxy, 2.07 Å; oxy, 2.16 Å) distances for MB/HB in the three states and at 20/260 K deviated by <0.02 Å, and the distances in the first and second iron coordination spheres mostly agreed within <0.05 Å with crystal structures (*SI Appendix*, Table S2). These results verified near-quantitative (>90%) presence of deoxy, carboxy, and oxy hemes and showed that the iron site configurations in MB and HB are similar and independent of the temperature.

Spin States from Kβ XES. Nonresonantly excited Kβ main-line emission spectra of HB and MB with deoxy, carboxy, and oxy hemes were collected at 20 K and 260 K by using an energy-sampling approach (Fig. 2) (44). As references for Kβ spectral features, three synthetic iron-porphyrin compounds [**1**, LS Fe(II); **2**, HS Fe(II); **3**, HS Fe(III)] and several nonporphyrin iron complexes with known spin and redox states were studied (*SI Appendix*, Figs. S7 and S14). At both temperatures, the spectral shapes for MB and HB were similar and the Kβ$_{1,3}$ line energies (deoxy, 7,058.6 eV; carboxy, 7,058.0 eV; oxy, 7,058.4 eV; *SI Appendix*, Table S1) agreed within ±0.1 eV. Significant line-shape differences between the MB/HB heme species and the porphyrins, i.e., variations in the relative Kβ$_{1,3}$ amplitudes at increasing energies for carboxy, deoxy, and oxy and of the Kβ' feature at ~7,045 eV, reflected iron-spin and redox-state differences. Both proteins in all states and the porphyrins showed temperature-independent Kβ spectra (Fig. 2 and *SI Appendix*, Fig. S6). The Kβ' amplitudes for MB/HB, porphyrins, and nonporphyrin compounds were determined and plotted versus the formal number of unpaired Fe(d) spins (Fig. 3). For porphyrin and nonporphyrin compounds, the doubling of the Kβ' amplitude for a Fe(d) spin count increase from 0 in LS Fe(II) to 5 in HS Fe(III) was well described by a linear relation. The Kβ' amplitudes of deoxy MB/HB agreed well with a Fe(d) count of 4 as in compound **2**, indicating HS Fe(II). The Kβ' amplitudes of carboxy MB/HB were centered close to 0 unpaired Fe(d) spins in LS Fe(II) as in
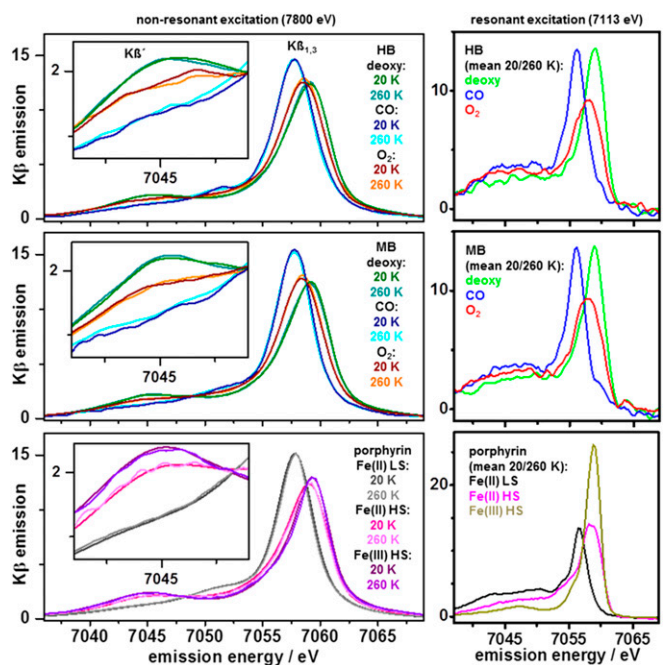

Fig. 2. Kβ emission spectra of MB, HB, and porphyrin references. (*Left*) Nonresonantly excited, normalized Kβ main-line spectra at 20 K or 260 K and magnified Kβ' feature in *Inset* (*Top*, MB solution; *Middle*, HB solution; *Bottom*, porphyrin compounds **1–3**). (*Right*) Resonantly excited, normalized Kβ main-line spectra (mean of data at 20 K and 260 K).
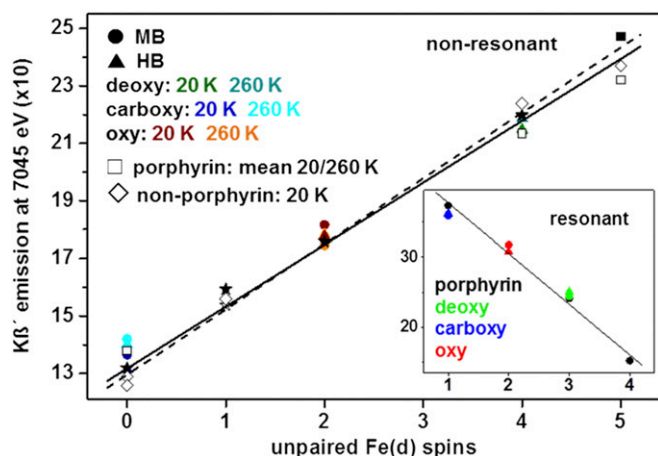
Fig. 3. Correlation of Kβ′ intensity and formal unpaired Fe(d) spin count. Data points refer to Kβ spectra in Fig. 2 (*Left*) and *SI Appendix*, Fig. S7 (nonporphyrin compounds). Kβ data for dehydrated deoxy, carboxy, and oxy HB and met (at Fe(d) = 1) MB/HB (solid asterisks) and solid hemin (solid square) at room temperature derived from ref. 45 were scaled to our data at Fe(d) = 0. Fe(d) spins correspond to: 0, LS Fe(II); 1, LS Fe(III); 4, HS Fe(II); and 5, HS Fe(III). Kβ′ intensities for oxy MB/HB were placed at Fe(d) = 2 for a formal IS Fe(II) (solid or dashed lines, linear fits to porphyrin/nonporphyrin data, R = 0.99). (*Inset*) Data from Kβ spectra in Fig. 2, *Right* (for Fe(d) count calculation see the text; line, linear fit to porphyrin data, R = 0.98).

compound **1**. For oxy MB/HB, the Kβ' amplitudes varied within only ~5%, and the mean value was in best agreement with an Fe(d) spin count of 2. We note that the hypothetical conversion of the Kβ' amplitude of oxy HB/MB to the smaller Kβ' amplitude for 1 spin [as for LS Fe(III)] required subtraction of a large (~40%) theoretical contribution of deoxy from the oxy spectra, which resulted in distorted line shapes (*SI Appendix*, Fig. S8). Such a large deoxy contribution further was unlikely regarding near-quantitative oxy formation as deduced from the optical absorption and XAS data. A LS Fe(III) contribution from met heme would even lead to underestimation of the Kβ' amplitude of oxy. An in-depth fit analysis of the Kβ spectra revealed detailed relations between peak energies/intensities and converged toward the same spin assignments as above (*SI Appendix*, Figs. S9–S11). These results strongly suggested that the HS Fe(II) in deoxy MB/HB is converted to an effective IS iron species in oxy upon O₂ binding.

A single earlier Kβ study on dried HB/MB at room temperature is available (45). Respective Kβ' amplitudes showed that HS Fe(III) in hemin and deoxy and carboxy HB were close to our data for Fe(d) counts of 5, 4, or 0, and the Fe(d) count of ~1 in met HB/MB agreed with LS Fe(III) dominance (42). The Kβ' amplitude of oxy HB suggested an Fe(d) count of 2, as did our data. The "IS" Fe(II) population in oxy thus seems not to depend on the protein hydration level and persists at ambient temperatures. Resonantly excited Kβ spectra were collected at an energy in the K-preedge region (Fig. 2). The spectra for MB/HB and the porphyrins revealed pronounced shape differences and larger Kβ' amplitudes for decreasing Fe(d) counts. A plot of the Kβ' amplitudes versus the by one unit diminished spin numbers due to a surplus Fe(d) electron showed an approximately linear relation for the porphyrins and positioned deoxy and carboxy MB/HB at values of 3 or 1 for HS or LS Fe(II) (Fig. 3). For oxy HB/MB, the Kβ' amplitudes close to 2 Fe(d) spins indicated a higher spin state than in carboxy. A mean spin count of 2 was calculated for 1s excitation, resulting in a surplus spin in the initially unoccupied d-levels or in spin pairing [Fe(d) = 3 or 1, see *SI Appendix* for further discussion], which supported an effective IS iron ion in oxy.

X-Ray–Induced Ligation Changes. X-ray fluorescence time traces were recorded at a fixed excitation energy in the K-edge rise to monitor radiation-induced changes at the iron centers (Fig. 4).

Similar kinetic behavior was observed for MB and HB. At 20 K, the deoxy K-edge energy remained almost unchanged during ~3.5 min of X-ray exposure because of the absence of photoreduction of the ferrous iron. For carboxy and oxy, a biphasic increase ($t_{1/2}$ ~5/75 s or ~10/150 s) of the fluorescence level due to an edge energy decrease to the deoxy level was observed and Kβ main-line emission, preedge absorption, and XANES spectra after ~150 s of X-ray exposure revealed that the resulting states showed similar spectral features as deoxy (*SI Appendix*, Fig. S12). At 260 K, the deoxy fluorescence decreased to the carboxy level within ~3.5 min ($t_{1/2}$ ~25 s) (Fig. 4) and final carboxy formation was revealed by Kβ main-line emission, preedge absorption, and XANES spectra (*SI Appendix*, Fig. S12). For carboxy, however, the X-ray fluorescence and, thus, the K-edge energy, as well as the Kβ and XANES features remained unchanged for ~3.5 min of X-ray exposure. Notably, porphyrin compound **3** showed no X-ray photoreduction at 20 K and monophasic Fe(III) to Fe(II) reduction at 260 K within ~5 min (*SI Appendix*, Fig. S12). For oxy, the K-edge energy shifts according to the fluorescence traces and the Kβ/XANES spectra after ~20 s and ~150 s of X-ray exposure suggested initial formation of deoxy ($t_{1/2}$ ~8 s) followed by carboxy formation ($t_{1/2}$ ~18 s). In particular, the oxy emission revealed an initial increase of the Kβ' amplitude, which was expected for deoxy formation, but not deoxy to carboxy conversion. The 260 K data for oxy were explainable by initial reduction and detachment of the O₂ ligand, followed by binding of a mobile CO species to the vacancy, whereas similarly fast CO binding than detachment explained the invariant data for carboxy. Mobile CO species may be created for example by X-ray induced decarboxylation of amino acid side chains or CO photolysis (46, 47). At 20 K, carbon oxide species were immobile and rebinding was impaired. The biphasic kinetics in carboxy and oxy suggested a similar two-step ligand-centered reduction, which seems incompatible with an initial true superoxide ligand in oxy.

Electronic Structure and Bonding. High-resolution preedge absorption (ctv) and nonresonantly excited Kβ satellite emission (vtc) spectra were collected on MB/HB (*SI Appendix*, Fig. S13) and the porphyrins. Spectral features were almost identical at 20/260 K and similar for MB/HB, which justified averaging to obtain mean ctv/vtc spectra of the porphyrins (*SI Appendix*, Fig. S14) and the heme species (Fig. 5). Subtle ctv differences of MB/HB were emphasized by narrow-band Kβ₁,₃ emission detection (*SI Appendix*, Fig. S13). The ctv spectra of the hemes showed two to three peaks varying ~1 eV in energy and ~twofold in intensity. The vtc spectra showed ~1 eV energy differences and Kβ₂,₅ intensity variations (Fig. 5). ctv
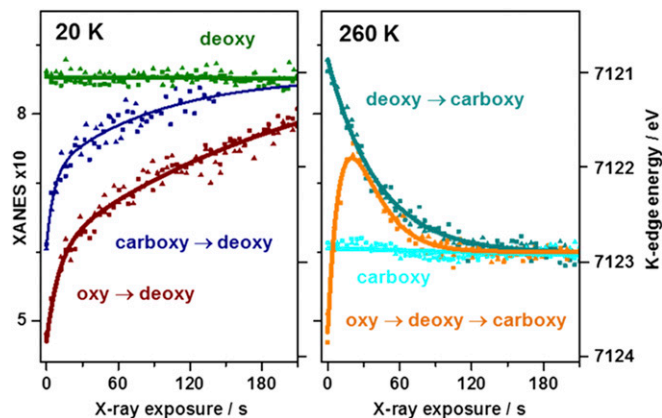

Fig. 4. Heme state conversion during X-ray exposure. Fluorescence changes monitored at 7,123 eV in the XANES (*SI Appendix*, Fig. S13) for indicated starting species in MB/HB (triangles/squares) at 20/260 K (*Left/Right*), K-edge amplitudes/energies shown on left/right y axes. Time traces correspond to ctv, XANES, and Kβ main-line changes (*SI Appendix*, Fig. S12) due to transitions between heme species. Lines: biexponential (carboxy/oxy, 20 K; oxy, 260 K), monoexponential (deoxy, 260 K), or linear (deoxy, 20 K; carboxy, 260 K) fits.
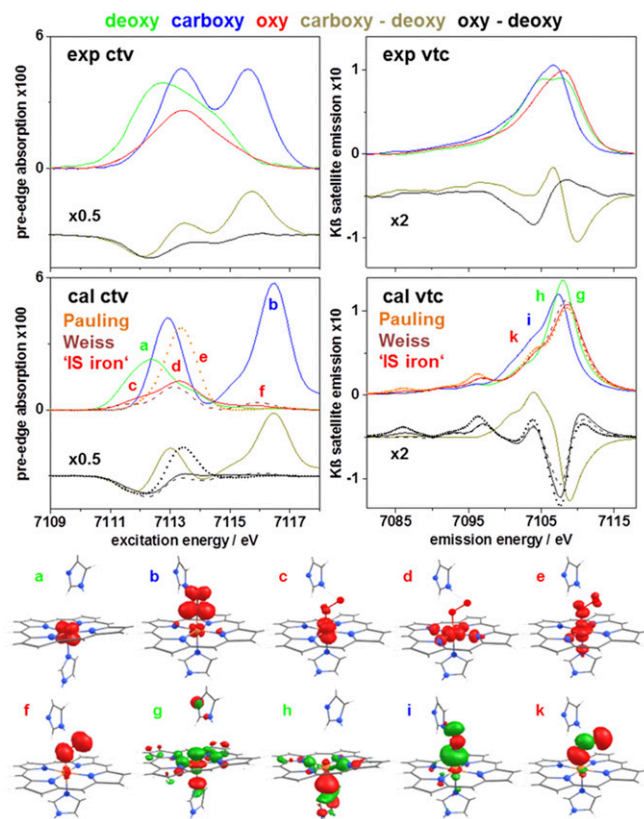
Fig. 5. Electronic excitation and decay transitions. (*Top*) Experimental ctv/vtc spectra (background-corrected mean MB/HB spectra/differences at 20/260K, individual spectra in *SI Appendix*, Fig. S13). (*Middle*) ctv/vtc spectra from (TD)DFT (vtc area-normalized; mean spectra of relaxed MB/HB heme structures correspond to deoxy, HS Fe(II); carboxy, LS Fe(II); and oxy, LS Fe(II) (Pauling), LS Fe(III) (Weiss), or to a mean of 2 Fe(d) spins ('IS iron'; *SI Appendix*, Figs. S17 and S18). (*Bottom*) Representative target/source MOs for transitions in spectral regions a–k.

spectra were collected by using narrow-band (7,045 eV) Kβ' emission detection. For the HS porphyrins, in contrast to the Kα- or Kβ$_{1,3}$-detected spectra, small ctv amplitudes reflected impaired 1s α-electron excitation due to the occupied α-spin valence levels, whereas for the LS porphyrin, Kβ$_{1,3}$- and Kβ'-detected spectra were similar because of similar 1s excitation into unoccupied levels (*SI Appendix*, Fig. S14). MB/HB showed similar Kβ'-detected ctv spectra (*SI Appendix*, Fig. S15). Negligible or similar ctv amplitudes vs. the Kα-detected spectra agreed with HS Fe(II) in deoxy and LS Fe(II) in carboxy. Smaller amplitudes vs. the Kα-detected spectra indicated a higher or lower spin state in oxy vs. carboxy or deoxy, further supporting two unpaired spins in oxy.

(TD)DFT was used to simulate ctv/vtc spectra. Calculated spectra for the porphyrins matched the experimental data well, which confirmed the spin states, revealed spin density distributions, and attributed target/source molecular orbitals (MOs) to excitation/decay transitions (*SI Appendix*, Fig. S16). For MB/HB, ctv spectra for HS Fe(II) in deoxy and LS Fe(II) in carboxy for calculations on crystal structures agreed reasonably with the experiment (*SI Appendix*, Fig. S17) and improvement resulted from geometry optimization (Fig. 5), yielding bond lengths/angles in excellent agreement with EXAFS (*SI Appendix*, Table S3). For deoxy, the ctv features reflected transitions mostly into Fe(d)-centered MOs, and the vtc features for decreasing energies were dominated by decay from MOs centered at iron, histidine, or heme; the spin density was located mostly on iron (*SI Appendix*, Fig. S18). For carboxy, two ctv peaks reflected transitions into Fe(d) or CO dominated MOs and increased lower-energy vtc

intensity was due to decay from CO-centered MOs (*SI Appendix*, Fig. S18). For oxy, depending on whether a nonafc or afc solution (within the "broken-symmetry" DFT formalism) was searched, Pauling or Weiss models emerged and a canonical IS Fe(II) was not produced even for extensive Fe-O$_2$ geometry variation (*SI Appendix*, Fig. S19). The structures showed similar vtc spectra with increased lower-energy intensity because of decay from O$_2$-centered MOs. A single large ctv peak for the Pauling model disagreed with the experiment. Three ctv features for the Weiss model were in better agreement and because of a lowest-energy transition into the Fe(d$_{yz}$) LUMO, intermediate transitions into Fe(d$_{x^2-y^2}$) and Fe(d$_{z^2}$) dominated MOs, and a highest-energy transition into an O$_2$-centered MO (Fig. 5). The ctv/vtc spectra for a mean of 2 Fe(d) spins, as estimated from (TD)DFT calculations for increasing spin states (*SI Appendix*, Fig. S17), were expected to be compatible with the experimental data (Fig. 5). A method for calculation of ctv/vtc spectra from a CASSCF wavefunction (below) is not available, but the respective MO occupancies suggested that the expected ctv transitions would yield three main ctv features, similar to the TDDFT and experimental spectra of oxy (*SI Appendix*, Fig. S18).

CASSCF calculations were carried out on porphyrin and heme structures (*SI Appendix*, Tables S4–S6 and Fig. S20), and spin densities (SD) in the natural molecular orbitals and effective unpaired electron densities (EUED = SD × (2 − SD)) (48) on iron and ligands were determined from the wavefunctions. Three double-occupied Fe(d) MOs for the porphyrin (**1**) and heme (carboxy) LS Fe(II) species and four or five single-occupied MOs for the Fe(II) (deoxy, **2**) or Fe(III) (**3**) HS species, and almost integer EUEDs on iron (0, 4, or 5) were in full agreement with the formal redox/spin states (Table 1). The oxy wavefunction was dominated (∼90%) by two contributions, both with unoccupied (SD < 0.05) Fe(d$_{z^2}$) and Fe(d$_{x^2-y^2}$) MOs and a double-occupied MO representing a polarized dative σ(Fe-O) bond with major O(p) and weak Fe(d$_{z^2}$) contributions (Fig. 6). MOs representing π and π* Fe-O (back-)bonds showed dominant Fe(d$_{yz}$) and weaker O(p) contributions and double/zero or zero/double occupancy in the two configurations; a double-occupied MO with dominant Fe(d$_{xz}$) and minor O(p) contributions indicates further delocalized π(Fe-O) backbonding (*SI Appendix*, Table S5). The SD in the two Fe(d$_{yz}$)-dominated MOs was ∼1.3 and ∼0.7 (EUED ∼0.89 and ∼0.91), revealing essentially two spatially separated unpaired spins in oxy, independent of, e.g., moderate Fe-O$_2$ bond length variations (*SI Appendix*, Fig. S20). The latter values together with the small EUEDs in the other Fe-assigned MOs yielded a total EUED on iron of ∼2.0, which summed up with the EUED on O$_2$ (∼0.3) to a value of ∼2.3, close to the EUED (∼2.4) for the ozone radical (O$_3^+$) (48).

Discussion

We used Fe Kβ-XES and K-edge XAS as well as quantum chemistry to study molecular and electronic structures of heme

Table 1. Effective unpaired electron density from CASSCF

Species	Redox and spin state	EUED	
		Fe	Ligand*
Heme			
deoxy	Fe(II) HS	4.000 (4)	—
carboxy	Fe(II) LS	0.001 (0)	0.352
oxy	Fe(II) IS†	2.014 (2)	0.302
Porphyrin			
1	Fe(II) LS	0.000 (0)	0.000
2	Fe(II) HS	4.000 (4)	0.092
3	Fe(III) HS	5.000 (5)	0.001

*Axial CO (carboxy), O$_2$ (oxy), N$_{Py}$ (1), O$_{THF}$ (2), or Cl$^−$ (3) ligand on top of the porphyrin in Fig. 1 and *SI Appendix*, Fig. S14.
†Simplified annotation (see text); formal unpaired Fe(d) spins in parentheses. The EUED on the ring systems in all heme and porphyrin species was zero.
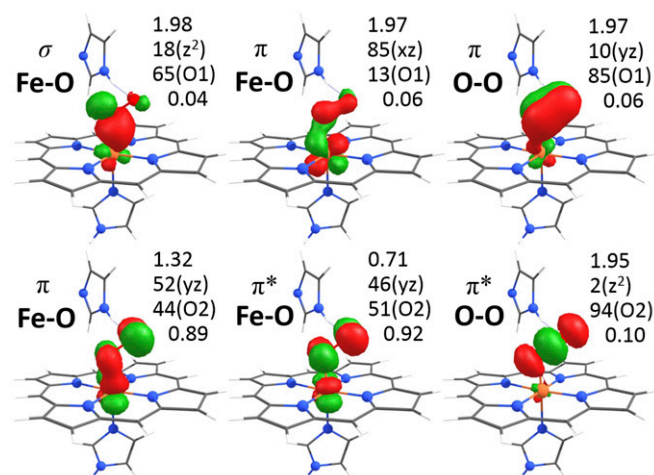
Fig. 6. Iron-oxygen bonding in oxy heme. Indicated spin densities, Fe(d) and O(p) characters (main contribution in parenthesis, O1 is Fe-bound), and EUEDs refer to (clockwise) MOs 2, 4, 3, 5, 7, 6 from CASSCF (14, 11) calculations (Table 1 and *SI Appendix*, Fig. S20). σ-donation and delocalized π/π* backbonding stabilize the O_2 ligand. For further analysis, see text and *SI Appendix*, Table S5.

species in MB and HB solutions. Fast spectral changes for all species even at cryogenic temperatures mandated rapid-scan XAS and energy-sampling XES approaches for unperturbed data collection. Apparent bond lengths and angle variations particularly in crystal structures of oxy globins likely relate to such radiation-induced modifications (41). We interpret our data as sequential ligand-centered two-electron reduction (at 20 K) of CO or O_2 and product detachment to form apparent deoxy heme (46, 47, 49). The similar kinetic behavior of carboxy and oxy implies similar electron uptake capability of both ligands, which is in agreement with the absence of a superoxide ligand, thereby supporting our computational results and the redox/spin state assignment for oxy.

Similar metrical, electronic, and kinetic parameters indicated similar metal site configurations in MB and HB. A significant influence of amino acid environment or hydrogen-bonding variations in the two heme proteins on these parameters of the iron centers and on the ligand bonding is unlikely, which agrees with earlier spectroscopic studies (50–53). Heme side-chain orientation differences in MB/HB presumably were reflected in the XANES by slight virtual level, i.e., Fe(4p), energy changes (54). All relevant heme features in MB/HB were invariant within 20–260 K, excluding population of higher spin states even far above the protein glass-transition point (~200 K) (55). This finding and, e.g., gradual spin crossover in iron porphyrins (56–58) suggest that also at room temperature, the spin state in the three heme species is the same and, therefore, physiologically relevant.

Kβ spectra of MB/HB and porphyrin compounds revealed a direct correlation of the formal unpaired Fe(d) spin count to the relative Kβ' intensity, in agreement with results for other iron species (32, 34), establishing further that the iron-centered radiative 3p→1s decay is a reliable probe of the valence level configuration. The steep correlation locates the overall iron bonding in the MB/HB hemes and the porphyrins closer to the noncovalent than covalent limit (32, 34, 59, 60). Agreement of our and earlier Kβ data of MB/HB (45) supports the spin state changes. For the hemes and porphyrins, our Kβ main-line, ctv/vtc, and (TD)DFT/CASSCF data revealed ferrous HS (deoxy, **2**) or LS (carboxy, **1**) and ferric HS (**3**) species (1, 40), emphasizing the method´s sensitivity for valence and spin-state discrimination. Further discussion of relations between the XAS/XES data and iron spin states is given in *SI Appendix*.

For oxy, the Kβ spectra indicated two unpaired Fe(d) spins on iron, which was compatible with the ctv/vtc data, by definition implying an IS metal center, as suggested by McClure/Goddard (15, 16). No significantly decreased ligand character of Fe(d) levels

in oxy vs. deoxy/carboxy in the calculations rendered diminished iron-porphyrin bonding covalency as an explanation for the Kβ data of oxy unlikely. The Pauling model with a LS Fe(II) and an innocent O_2 ligand (13) was essentially excluded (and higher spin states, M > 1) by our data, strengthening previous conclusions (36, 40). DFT converged to the Weiss model with a ferric iron and a superoxide ligand (17) and yielded ctv/vtc spectra more close to our and earlier data (36, 40), but this preference reflected over-estimation of metal-to-ligand charge transfer (22, 23). CASSCF on oxy yielded a two-component wavefunction as found earlier (21–23). It comprised in effect two unpaired spins on iron, in perfect agreement with our Kβ data, thereby benchmarking the quantum chemical prediction and providing a quantitative link between theory and spectroscopy. The emerging bonding situation includes an essentially ferrous iron center, little charge transfer to O_2 and minor superoxide character of the noninnocent ligand, significant double-bond properties of the Fe–O_2 interaction, and three-center ozone-like electron delocalization. It combines the classical models into a more realistic view of O_2 bonding in MB/HB, featuring limited radical character and delocalized backbonding stabilization of the ligand as prerequisites for reversible O_2 transport.

Materials and Methods

1. Kepp KP (2016) Heme: From quantum spin crossover to oxygen manager of life. *Coord Chem Rev* 344:363–374.
2. Reeder BJ, Svistunenko DA, Cooper CE, Wilson MT (2004) The radical and redox chemistry of myoglobin and hemoglobin: From in vitro studies to human pathology. *Antioxid Redox Signal* 6:954–966.
3. Bren KL, Eisenberg R, Gray HB (2015) Discovery of the magnetic behavior of hemoglobin: A beginning of bioinorganic chemistry. *Proc Natl Acad Sci USA* 112:13123–13127.
4. Bewley KD, Ellis KE, Firer-Sherwood MA, Elliott SJ (2013) Multi-heme proteins: Nature's electronic multi-purpose tool. *Biochim Biophys Acta* 1827:938–948.
5. Poulos TL (2014) Heme enzyme structure and function. *Chem Rev* 114:3919–3962.
6. Weber RE, Vinogradov SN (2001) Nonvertebrate hemoglobins: Functions and molecular adaptations. *Physiol Rev* 81:569–628.
7. Frey AD, Kallio PT (2003) Bacterial hemoglobins and flavohemoglobins: Versatile proteins and their impact on microbiology and biotechnology. *FEMS Microbiol Rev* 27:525–545.
8. Hoy JA, Hargrove MS (2008) The structure and function of plant hemoglobins. *Plant Physiol Biochem* 46:371–379.
9. Brunori M (1999) Hemoglobin is an honorary enzyme. *Trends Biochem Sci* 24:158–161.
10. Park SY, Yokoyama T, Shibayama N, Shiro Y, Tame JRH (2006) 1.25 A resolution crystal structures of human haemoglobin in the oxy, deoxy and carbonmonoxy forms. *J Mol Biol* 360:690–701.
11. Vojtechovský J, Chu K, Berendzen J, Sweet RM, Schlichting I (1999) Crystal structures of myoglobin-ligand complexes at near-atomic resolution. *Biophys J* 77:2153–2174.
12. Weissbluth M (1975) *Hemoglobin: Cooperativity and Electronic Properties* (Springer, Berlin).
13. Pauling L, Coryell CD (1936) The magnetic properties and structure of hemoglobin, oxyhemoglobin and carbonmonoxyhemoglobin. *Proc Natl Acad Sci USA* 22:210–216.
14. Pauling L (1977) Magnetic properties and structure of oxyhemoglobin. *Proc Natl Acad Sci USA* 74:2612–2613.
15. McClure DS (1960) Electronic structure of transition-metal complex ions. *Radiat Res Suppl* 2:218–242.
16. Goddard WA, 3rd, Olafson BD (1975) Ozone model for bonding of an O2 to heme in oxyhemoglobin. *Proc Natl Acad Sci USA* 72:2335–2339.
17. Weiss JJ (1964) Nature of the iron-oxygen bond in oxyhaemoglobin. *Nature* 203:182–183.
18. Harcourt RD (2016) Transition metal complexes with CO, N2, NO and O2 ligands. *Bonding in Electron-Rich Molecules*, ed Harcourt RD (Springer, New York), pp 231–246.
19. Shaik S, Chen H (2011) Lessons on O2 and NO bonding to heme from ab initio multireference/multiconfiguration and DFT calculations. *J Biol Inorg Chem* 16:841–855.
20. Kepp KP (2013) Consistent descriptions of metal-ligand bonds and spin-crossover in inorganic chemistry. *Coord Chem Rev* 257:196–209.
21. Yamamoto S, Kashiwagi H (1993) Casscf calculation on dioxygen heme complex with extended basis set. *Chem Phys Lett* 205:306–312.
22. Chen H, Ikeda-Saito M, Shaik S (2008) Nature of the Fe-O2 bonding in oxy-myoglobin: Effect of the protein. *J Am Chem Soc* 130:14778–14790.
23. Jensen KP, Roos BO, Ryde U (2005) O2-binding to heme: Electronic structure and spectrum of oxyheme, studied by multiconfigurational methods. *J Inorg Biochem* 99:45–54.
24. Yonetani T, Kanaori K (2013) How does hemoglobin generate such diverse functionality of physiological relevance? *Biochim Biophys Acta* 1834:1873–1884.
25. Shikama K (2006) Nature of the FeO2 bonding in myoglobin and hemoglobin: A new molecular paradigm. *Prog Biophys Mol Biol* 91:83–162.
26. Perutz MF (1989) Myoglobin and haemoglobin: Role of distal residues in reactions with haem ligands. *Trends Biochem Sci* 14:42–44.
27. Glatzel P, Bergmann U (2005) High resolution 1s core hole X-ray spectroscopy in 3d transition metal complexes - electronic and structural information. *Coord Chem Rev* 249:65–95.
28. De Groot F, Kotani A (2008) *Core Level Spectroscopy of Solids* (Taylor & Francis CRC, Boca Raton, FL).
29. van Bokhoven JA, Lamberti C (2016) *X-Ray Absorption and X-Ray Emission Spectroscopy: Theory and Applications* (Wiley, New York).
30. Pollock CJ, DeBeer S (2015) Insights into the geometric and electronic structure of transition metal centers from valence-to-core X-ray emission spectroscopy. *Acc Chem Res* 48:2967–2975.
31. Lehnert N, George SD, Solomon EI (2001) Recent advances in bioinorganic spectroscopy. *Curr Opin Chem Biol* 5:176–187.
32. Pollock CJ, Delgado-Jaime MU, Atanasov M, Neese F, DeBeer S (2014) Kβ mainline X-ray emission spectroscopy as an experimental probe of metal-ligand covalency. *J Am Chem Soc* 136:9453–9463.
33. deGroot FMF (2000) Site-Selective XAFS: A new tool for catalysis research. *Topics in Catalysis* 10:179–186.
34. Mebs S, Braun B, Kositzki R, Limberg C, Haumann M (2015) Abrupt versus gradual spin-crossover in Fe(II)(phen)2(NCS)2 and Fe(III)(dedtc)3 compared by X-ray absorption and emission spectroscopy and quantum-chemical calculations. *Inorg Chem* 54:11606–11624.
35. Pin S, Alpert B, Congiucastellano A, Longa SD, Bianconi A (1994) X-ray-absorption spectroscopy of hemoglobin. *Hemoglobins. Pt C* 232:266–292.
36. Lima FA, et al. (2014) Probing the electronic and geometric structure of ferric and ferrous myoglobins in physiological solutions by Fe K-edge absorption spectroscopy. *Phys Chem Chem Phys* 16:1617–1631.
37. Eisenberger P, Shulman RG, Brown GS, Ogawa S (1976) Structure-function relations in hemoglobin as determined by x-ray absorption spectroscopy. *Proc Natl Acad Sci USA* 73:491–495.
38. Durham P, et al. (1983) X-ray absorption near edge structure (XANES) for CO, CN and deoxyhaemoglobin: Geometrical information. *EMBO J* 2:1441–1443.
39. Zhang K, Reddy KS, Bunker G, Chance B (1991) Active site conformation in myoglobin as determined by X-ray absorption spectroscopy. *Proteins* 10:279–286.
40. Wilson SA, et al. (2013) X-ray absorption spectroscopic investigation of the electronic structure differences in solution and crystalline oxyhemoglobin. *Proc Natl Acad Sci USA* 110:16333–16338.
41. Hersleth HP, Andersson KK (2011) How different oxidation states of crystalline myoglobin are influenced by X-rays. *Biochim Biophys Acta* 1814:785–796.
42. Feis A, Marzocchi MP, Paoli M, Smulevich G (1994) Spin state and axial ligand bonding in the hydroxide complexes of metmyoglobin, methemoglobin, and horseradish peroxidase at room and low temperatures. *Biochemistry* 33:4577–4583.
43. Ratanasopa K, Strader MB, Alayash AI, Bulow L (2015) Dissection of the radical reactions linked to fetal hemoglobin reveals enhanced pseudoperoxidase activity. *Front Physiol* 6:39.
44. Zaharieva I, et al. (2016) Room-temperature energy-sampling Kbeta X-ray emission spectroscopy of the Mn4Ca complex of photosynthesis reveals three manganese-centered oxidation steps and suggests a coordination change prior to O2 formation. *Biochemistry* 55:4197–4211.
45. Koster AS (1972) Electronic state of iron in hemoglobin, myoglobin and derivatives, as inferred from X-ray-fluorescence spectra. *J Chem Phys* 56:3161–3164.
46. Weik M, et al. (2000) Specific chemical and structural damage to proteins produced by synchrotron radiation. *Proc Natl Acad Sci USA* 97:623–628.
47. Liu B, et al. (2012) Structural changes that occur upon photolysis of the Fe(II)(a3)-CO complex in the cytochrome ba(3)-oxidase of *Thermus thermophilus*: A combined X-ray crystallographic and infrared spectral study demonstrates CO binding to Cu(B). *Biochim Biophys Acta* 1817:658–665.
48. Takatsuka K, Fueno T, Yamaguchi K (1978) Distribution of odd electrons in ground-state molecules. *Theor Chim Acta* 48:175–183.
49. Della Longa S, Arcovito A (2010) X-ray-induced lysis of the Fe-CO bond in carbon-monoxy-myoglobin. *Inorg Chem* 49:9958–9961.
50. Tilton RF, Jr, Kuntz ID, Jr (1982) Nuclear magnetic resonance studies of xenon-129 with myoglobin and hemoglobin. *Biochemistry* 21:6850–6857.
51. Sharonov YA, et al. (1978) Magnetic circular dichroism studies of myoglobin, hemoglobin and peroxidase at room and low temperatures. Ferrous high spin derivatives. *Biophys Struct Mech* 4:139–158.
52. Yoshida S, Iizuka T, Nozawa T, Hatano M (1975) Studies on the charge transfer band in high spin state of ferric myoglobin and hemoglobin by low temperature optical and magnetic circular dichroism spectroscopy. *Biochim Biophys Acta* 405:122–135.
53. Tsubaki M, Srivastava RB, Yu NT (1982) Resonance Raman investigation of carbon monoxide bonding in (carbon monoxy)hemoglobin and -myoglobin: Detection of Fe-CO stretching and Fe-C-O bending vibrations and influence of the quaternary structure change. *Biochemistry* 21:1132–1140.
54. Brown WE, 3rd, Sutcliffe JW, Pulsinelli PD (1983) Multiple internal reflectance infrared spectra of variably hydrated hemoglobin and myoglobin films: Effects of globin hydration on ligand conformer dynamics and reactivity at the heme. *Biochemistry* 22:2914–2923.
55. Demmel F, Doster W, Petry W, Schulte A (1997) Vibrational frequency shifts as a probe of hydrogen bonds: Thermal expansion and glass transition of myoglobin in mixed solvents. *Eur Biophys J* 26:327–335.
56. Piruzian LA, Kuznetsov AA, Chikov VM, Plotnikova IG (1984) Temperature dependence of the magnetic susceptibility of oxy- and carboxyhemoglobin in the erythrocytes. *Izvest Akad Nauk SSSR* 6:894–900.
57. Kent TA, et al. (1979) High magnetic field Mössbauer studies of deoxymyoglobin, deoxyhemoglobin, and synthetic analogues. *Biochim Biophys Acta* 580:245–258.
58. Ikeue T, et al. (2001) Saddle-shaped six-coordinate iron(III) porphyrin complexes showing a novel spin crossover between S=1/2 and S=3/2 spin states. *Angew Chem Int Ed Engl* 40:2617–2620.
59. Kroll T, et al. (2014) Resonant inelastic X-ray scattering on ferrous and ferric bis-imidazole porphyrin and cytochrome c: Nature and role of the axial methionine-Fe bond. *J Am Chem Soc* 136:18087–18099.
60. Lundberg M, et al. (2013) Metal-ligand covalency of iron complexes from high-resolution resonant inelastic X-ray scattering. *J Am Chem Soc* 135:17121–17134.
61. Scheidt WR, Osvath SR, Lee YJ (1987) Crystal and molecular-structure of bis(Imidazole)(meso-tetraphenylporphinato)iron(III) chloride - a classic molecule revisited. *J Am Chem Soc* 109:1958–1963.
62. Di Iorio EE (1981) Preparation of derivatives of ferrous and ferric hemoglobin. *Methods Enzymol* 76:57–72.
63. Huwald D, Schrapers P, Kositzki R, Haumann M, Hemschemeier A (2015) Characterization of unusual truncated hemoglobins of *Chlamydomonas reinhardtii* suggests specialized functions. *Planta* 242:167–185.
64. Rehr JJ, Kas JJ, Vila FD, Prange MP, Jorissen K (2010) Parameter-free calculations of X-ray spectra with FEFF9. *Phys Chem Chem Phys* 12:5503–5513.
65. Neese F (2012) The ORCA program system. *Wires Comput Mol Sci* 2:73–78.
66. Frisch MJT, et al. (2009) *Gaussian 09, Revision D.01* (Gaussian, Wallingford, CT).
67. Kositzki R, et al. (2016) Protonation state of MnFe and FeFe cofactors in a ligand binding oxidase revealed by X-ray absorption, emission, and vibrational spectroscopy and QM/MM calculations. *Inorg Chem* 55:9869–9885.
68. Phillips SEV, Schoenborn BP (1981) Neutron diffraction reveals oxygen-histidine hydrogen bond in oxymyoglobin. *Nature* 292:81–82.

BIOPHYSICS AND COMPUTATIONAL BIOLOGY